Plasmas sustained in bubbles in water: optical emission and excitation mechanisms

Wei Tian[1], Kunhide Tachibana[2] and Mark J Kushner[3,4]

[1] Department of Nuclear Engineering and Radiological Science, University of Michigan, Ann Arbor, MI 48109-2104, USA
[2] Osaka Electro-Communication University, Neyagawa, Osaka 572-8530, Japan
[3] Department of Electrical Engineering and Computer Science, University of Michigan, Ann Arbor, MI 48109-2122, USA

E-mail: bucktian@umich.edu, kunihide@isc.osakac.ac.jp and mjkush@umich.edu

Abstract

Plasmas in bubbles in water are being investigated for their ability to produce chemically reactive species for water purification and medical treatment. The gas forming the bubble is potentially a design parameter for water purification as the type and rate of production of active species may be controllable by the type of gas in the bubble. In this paper, we report on a computational investigation of the dynamics of plasmas in bubbles in water sustained in different gases. Images, optical spectra and plasma properties are discussed for plasmas in bubbles of N_2, Ar and He in water, and compared to experiments. The differences in plasma dynamics and spatial distribution of the plasma (e.g., volume discharge or surface hugging) when using different gases depend in large part on the electron energy relaxation length, and the rate of diffusion of water vapour into the interior of the bubble. Electron impact dissociative excitation of water vapour, electron impact excitation of dissociation products and excitation transfer from the plasma excited injected bubble gases to water vapour all contribute to plasma emission. Variations in the contributions of these processes are responsible for differences in the observed optical spectra and differences in radical production.

Keywords: plasmas in bubbles, plasmas in liquids, dielectric barrier discharge

(Some figures may appear in colour only in the online journal)

1. Introduction

Plasmas in or in contact with water are being investigated due to their ability to produce chemically reactive species such as hydrogen peroxide [1], hydroxyl radicals [2] and oxygen radicals [3] for applications ranging from environmental cleanup [3] and chemical processing [4] to healthcare [5]. Electric discharges in liquid have been reported in the absence of a vapour phase when using rapidly applied high voltages [6]. However, from the perspective of high average power industrial applications, it is likely that radical formation in discharges in liquids dominantly occurs in a pre-existing vapour phase or a

vapour phase produced by the discharge itself. Formation of the vapour phase by the discharge is energetically costly as the heat of formation of the gas must be invested before significant radical production occurs. High voltages are also required to produce the requisite E/N (electric field/gas number density) to produce the discharge in a liquid, whose densities are typically 1000 times that of atmospheric pressure gas.

An alternative approach is to inject atmospheric pressure bubbles into the liquid and sustain the discharge in the bubbles. Due to the low molecular density in the bubble compared to the liquid, a significantly lower voltage will initiate the plasma in the bubble compared to the liquid. For sufficiently small bubbles and residence times of the bubble in the liquid, the majority of radicals produced in the bubble will likely diffuse

[4] Author to whom any correspondence should be addressed.

1

J. Phys. D: Appl. Phys. **47** (2014) 055202

Wei Tian *et al*

into the liquid. The composition of the radicals produced in the bubble is determined by the gas used to make the bubble and the vapour of the liquid that diffuses into the bubble. It has been proposed that initiating and propagating discharges in liquid are likely enabled (or at least enhanced) by pre-existing bubbles. Even in degassed water, there probably are pre-existing bubbles of 100's nm [7].

Discharges in bubbles in water are more complex than their counterparts in the gas phase due to the close proximity of the gas–water interface. In actual practice, discharges in bubbles can significantly deform and in some cases the bubble may burst [8]. Even in the absence of these morphological changes, the gas–vapour interface is critical to the characteristics of the plasma in a bubble, and, in particular, a plasma-in-a-bubble-in-water (PBW).

In one arrangement of PBW, the bubble is attached to an electrode immersed in water. The applied voltage is low enough that the discharge occurs only in the bubble (and not in the water). For initially deionized or low conductivity water, the water essentially operates as a dielectric on the timescales of the discharge pulse, and so the discharge is terminated when charge accumulates at the surface of the water, much like a dielectric barrier discharge (DBD). Prior modelling results [10] and experimental observations [11] have shown that under select conditions, the discharge in a PBW propagates along the vapour–water boundary. This surface-hugging-discharge mode is a consequence of the electric field enhancement that occurs across a curved boundary between two materials having different dielectric constants ($\varepsilon/\varepsilon_0 = 1$ for the bubble and 80 for water). These plasma dynamics fortunately concentrate the discharge power at the location where the water vapour density is likely highest and so the production of oxidizing radicals is large. PBWs can appear as both a volumetric dielectric barrier discharge [9] and as a surface discharge, the latter of which is a variant of a DBD [10, 11]. For large bubbles, PBWs tend to hug the water surface whereas in smaller bubbles and with larger voltages, the discharge tends to more uniformly fill the bubble.

With the goal of quantifying the basic physical and chemical processes of PBW, in this paper, we discuss results from a computational investigation of the plasma dynamics of electrical discharges in idealized bubbles in water. A single discharge pulse is investigated in PBWs through He, Ar and N$_2$ filled bubbles. The bubbles are modelled as being static since the discharge occurs and evolves in nanoseconds, and so no deformation of the bubble occurs in the model [10]. The water is represented as a dielectric material so no reactions occur inside the water. Synthesized images and optical spectra from the bubbles are compared to recent experiments by Tachibana *et al* [11]. In these experiments, the bubbles were distorted by the discharges after the current pulse terminated. However, during the short current pulse, the bubbles were largely undisturbed. A new bubble was created for the next discharge pulse so the distortion of the previous bubble was not important. In this paper, we discuss excitation mechanisms in the bubble during the discharge pulse prior to distortions being important.

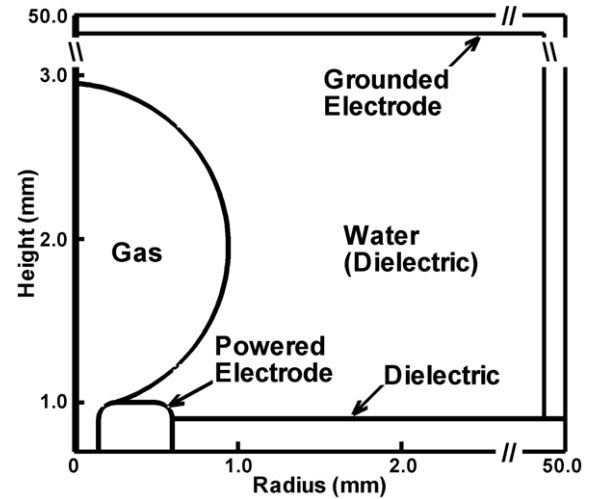We found that the electron temperature, T_e, within the PBW is higher for atomic gases and lower for molecular gases,

Figure 1. Schematic of the geometry highlighting the computational domain in the vicinity of the bubble. The domain is cylindrically symmetric across the left boundary.

which result in strong and weak optical emissions, respectively. In addition to differences in T_e, excitation transfer processes from the electronically excited bubble gases to water vapour also contribute to differences in the optical emission. These results are also influenced by the different rates of diffusion of water vapour from the surface of the water into the interior of the bubble. The electron energy relaxation length, λ_e, defined by the characteristic distance electrons travel before dissipating their energy through collisions, is affected by this diffusion of water vapour into the bubble.

The model used in this investigation is described in section 2 followed by a discussion of simulated PBW in section 3. Our concluding remarks are in section 4.

2. Description of model

The model used in this investigation, *nonPDPSIM*, is a two-dimensional plasma hydrodynamics simulation which is essentially the same as that described in [10, 12, 13]. and so will be only briefly described here. In the model, Poisson's equation, transport equations for all charged and neutral species and the electron energy equation are solved for electrical potential, density and momenta of charged and neutral species, and electron temperature, respectively. The electron transport and rate coefficient as a function of average electron energy are obtained by solving Boltzmann's equation using a two-term spherical harmonic expansion. Radiation transport and photon-induced ionization and dissociation are addressed by implementing a Green's function propagator. High lying excited states generate UV/VUV radiation, which is attenuated by absorption in propagating through the plasma [14]. Radiation transport also provides photon fluxes to surfaces. In these results, H$_2$O undergoes photoionization and photodissociation to H and OH.

The model geometry is shown in figure 1. The entire computational domain is 50 mm × 50 mm and is filled with water. (The bubble region is enlarged in figure 1). The system

J. Phys. D: Appl. Phys. **47** (2014) 055202

Wei Tian *et al*

is cylindrically symmetric across the centre line on the left boundary. The bubble having a diameter of 2 mm is attached to a metal tube having a 0.3 mm inner diameter which also serves as the powered electrode. The metal tube is covered with a 3.6 mm thick dielectric ($\varepsilon/\varepsilon_0 = 4$). Outside the bubble is water, which in our model is treated as a non-conductive material with a dielectric constant of $\varepsilon/\varepsilon_0 = 80$. Grounded metal electrodes are on the top and right boundaries, which are sufficiently far away from the bubble that the predicted plasma properties are not significantly affected by the precise location of the ground plane. The discharge is initiated and sustained inside the bubble. Charge is allowed to accumulate at the bubble–surface consistent with the incident plasma fluxes. This accumulation of charge is a good approximation if the dielectric relaxation time of the water is long compared to the time of propagation of the surface discharge within the bubble, which is about 10 ns. The conductivity that produces a dielectric relaxation time of 10 ns in water is $0.1\,\mathrm{S\,m^{-1}}$, which is typically a large conductivity compared to tap water. Secondary electron emission from the water is also taken into account when ions and photons strike the bubble–liquid interface. Our study addresses plasma dynamics on the nanosecond time scale, so deformation of the bubble, which takes place on microsecond time scales, is not considered.

A two-dimensional unstructured mesh is used for the numerical grid. The mesh consists of approximately 10 000 nodes, of which about 7000 nodes are in the plasma region inside the bubble and which is where the plasma transport equations are solved. The volume near the bubble–surface where the discharge propagates and strikes the water is refined to have elements with smaller dimensions than the more remote regions of the mesh. The smallest distances between the nodes in the gas phase in the centre of the bubble are about $50\,\mu$m, decreasing to less than $5\,\mu$m near the boundary. The sheath thickness near the surface of the water is estimated to be about 10–$20\,\mu$m so we are nominally resolving the sheath at that location. Near the electrode, the plasma density is higher and we are not resolving that sheath. However little optical emission comes from that location.

The discharge is initiated by seeding a neutral plasma of $10^9\,\mathrm{cm^{-3}}$ having a radius of $50\,\mu$m in the vicinity of the powered electrode. The discharge is then naturally sustained by the secondary emission from surfaces. The secondary emission coefficient is 0.15 for ions and 0.001 for photons. The water surface is initially uncharged. The applied voltage rises in 0.1 ns to 15 kV (or the charging voltage), remains constant for 15 ns, and drops to zero in 1 ns. The plasma computation then proceeds for 50 ns, which is a long enough time to capture the characteristics of the discharge while having a reasonable computation time.

There is a sensitivity on seeding level. If the density is too low (below the ambipolar limit) then the seed electrons freely diffuse and you lose them before the discharge can develop. By increasing the seeding level by a reasonable amount, you generally do not significantly affect the final outcome other than by reducing the discharge formation time. For these conditions, empirically we found $10^8\,\mathrm{cm^{-3}}$ to be a practical lower limit for the seeding level and $10^9\,\mathrm{cm^{-3}}$ to be a practical upper limit that does not affect the bubble dynamics.

Table 1. Lennard-Jones radius and binary diffusion coefficient of H_2O in each gas at 1 atm.

	Lennard-Jones Radius (Å) [16]	H_2O Diffusion coefficient (cm^2 s^{-1})
H_2O	2.52	0.51
He	2.58	0.66
Ar	3.42	0.20
N_2	3.68	0.23

In experiments by Tachibana [11], atmospheric pressure bubbles of He, Ar and N_2 were created in the water at the tip of the electrode followed by application of high voltage to create the discharge a few milliseconds later. A positive pulse of 15 kV with a 100 ns rise time was applied with a $5\,\mu$s pulse width. The short duration of the pulse prevented arcing. Due to the short time between creating the bubble and pulsing the discharge, water vapour is not likely to be uniformly saturating the gas. To address these conditions, water vapour in the model is allowed to diffuse into the bubble from the water boundary where its density is given by the saturated water vapour pressure at room temperature (27 Torr) [15]. Operationally, we assume that the bubble is formed at time $t = 0$ consisting only of the pure injected gas. Water vapour is then allowed to diffuse into the bubble for 1 ms prior to applying voltage. Binary diffusion coefficients, D_{12}, for H_2O through the fill gas of the bubbles were estimated using their Lennard-Jones parameters and modified hard-sphere collisions [16],

$$D_{12} = 0.001858 \sqrt{\frac{M_1 + M_2}{M_1 M_2}} \frac{T^{3/2}}{p\sigma_{12}^2 \Omega_D},$$

where T is the gas temperature (K), M_1 and M_2 are molecular weights of water and the gas within the bubble, p (atm) is the total pressure of the binary mixture, σ_{12} is the Lennard-Jones parameter defined by $\sigma_{12} = 1/2(\sigma_1 + \sigma_2)$, Ω_D is the temperature-dependent collision integral [16]. The Lennard-Jones parameters used here and the derived diffusion coefficients are listed in table 1.

Given the computational scale of the two-dimensional calculation, a reduced reaction mechanism was used for He, Ar and N_2 with added H_2O, and is shown in table 2. The reaction mechanism was chosen to be a self-consistent system that captures the pertinent plasma processes on the $<1\,\mu$s timescale and neutral processes on longer time scales, while also being compatible with the increased computational load of this 2D simulation. Ions which are unique for each gas fill of the bubble are He$^+$, He$_2^+$; Ar$^+$, Ar$_2^+$; and N_2^+, N_4^+. Ions which occur in all three gas fills are H_2O^+, H$^+$, OH$^+$, O$^-$ and OH$^-$. Excited states of the rare gases are intended to be lumped states. He*, He** and He*** are nominally He(2^3S), He(2^1P) and He(3^3P). Ar* represents the two metastable states of the Ar(1s) manifold, Ar(1s$_1$) and Ar(1s$_3$). Ar** represents the two radiative states of the manifold, Ar(1s$_2$) and Ar(1s$_4$). Ar*** nominally represents Ar(4p) and higher states. The states N_2^*, N_2^{**} and N_2^{***} are nominally $N_2(A)$ and $N_2(B)$; $N_2(a')$; $N_2(C)$ and higher states, respectively. The vibrationally excited states of N_2 were lumped into $N_2(v)$. The excited states of H and OH are also taken into account. H*, H**, H*** and OH*

Table 2. He/H_2O, Ar/H_2O and N_2/H_2O reaction mechanism.

Reaction	Rate Coefficient[a]	Ref.
He Reactions		
$e + He \rightarrow He + e$	b	[18]
$e + He \leftrightarrow He^* + e$	b,c	[19]
$e + He \leftrightarrow He^{**} + e$	b,c	[19]
$e + He \leftrightarrow He^{***} + e$	b,c	[19]
$e + He^* \leftrightarrow He^{**} + e$	b,c	[19]
$e + He^* \leftrightarrow He^{***} + e$	b,c	[19]
$e + He^{**} \leftrightarrow He^{***} + e$	b,c	[19]
$e + He \rightarrow He^+ + e + e$	b	[20]
$e + He^* \rightarrow He^+ + e + e$	b	[21]
$e + He^{**} \rightarrow He^+ + e + e$	b	[21]
$e + He^{***} \rightarrow He^+ + e + e$	b	[21]
$e + He^+ \rightarrow He^*$	$6.76 \times 10^{-13} T_e^{-0.5}$	[22]
$e + e + He^+ \rightarrow He^* + e$	$6.2 \times 10^{-27} T_e^{-4.4} \, cm^6 \, s^{-1}$	[22]
$e + He + He^+ \rightarrow He^* + He$	$6.6 \times 10^{-30} T_e^{-2} \, cm^6 \, s^{-1}$	[23]
$e + He_2^+ \rightarrow He^* + He$	$7.12 \times 10^{-15} (T_e/T_g)^{-1.5}$	[18]
$e + He + He_2^+ \rightarrow He_2^* + He$	$1.5 \times 10^{-27} \, cm^6 \, s^{-1}$	[18]
$e + He + He_2^+ \rightarrow He^* + He + He$	$3.5 \times 10^{-27} \, cm^6 \, s^{-1}$	[18]
$e + e + He_2^+ \rightarrow He_2^* + e$	$1.2 \times 10^{-21} \, cm^6 \, s^{-1}$	[18]
$e + e + He_2^+ \rightarrow He^* + He + e$	$2.8 \times 10^{-20} \, cm^6 \, s^{-1}$	[18]
$e + He_2^* \rightarrow He + He + e$	3.8×10^{-9}	[18]
$(He^*, He^{**}, He^{***}) + (He^*, He^{**}, He^{***})$ $\rightarrow He + He^+ + e$	$5 \times 10^{-10} T_n^{0.5}$	[18]d,e
$He^+ + He \rightarrow He + He^+$	$6 \times 10^{-10} T_n^{0.5}$	[24]
$He^+ + He + He \rightarrow He + He_2^+$	$1.41 \times 10^{-31} T_n^{-0.5} \, cm^6 \, s^{-1}$	[25]
$(He^*, He^{**}, He^{***}) + He + He \rightarrow He + He_2^*$	$1.6 \times 10^{-32} \, cm^6 \, s^{-1}$	[18]d,e
Ar Reactions		
$e + Ar \rightarrow Ar + e$	b	[26]
$e + Ar \leftrightarrow Ar^* + e$	b,c	[26]
$e + Ar \leftrightarrow Ar^{**} + e$	b,c	[26]
$e + Ar \leftrightarrow Ar^{***} + e$	b,c	[26]
$e + Ar^* \leftrightarrow Ar^{**} + e$	b,c	[26]
$e + Ar^* \leftrightarrow Ar^{***} + e$	b,c	[27]
$e + Ar^{**} \leftrightarrow Ar^{***} + e$	b,c	[27]
$e + Ar \rightarrow Ar^+ + e + e$	b	[20]
$e + Ar^* \rightarrow Ar^+ + e + e$	b	[28]
$e + Ar^{**} \rightarrow Ar^+ + e + e$	b	[28]
$e + Ar^{***} \rightarrow Ar^+ + e + e$	b	[21]
$e + Ar^+ \rightarrow Ar^{***}$	$4 \times 10^{-13} T_e^{-0.5}$	[29]
$e + e + Ar^+ \rightarrow Ar^{***} + e$	$5 \times 10^{-27} T_e^{-4.5} \, cm^6 \, s^{-1}$	[29]
$e + Ar_2^* \rightarrow Ar_2^+ + e + e$	$9 \times 10^{-8} T_e^{0.7}$	[30]
$e + Ar_2^* \rightarrow Ar + Ar + e$	1×10^{-7}	[30]
$e + Ar_2^+ \rightarrow Ar^{***} + Ar$	$5.38 \times 10^{-8} T_e^{-0.66}$	[30]
$(Ar^*, Ar^{**}, Ar^{***}) + (Ar^*, Ar^{**}, Ar^{***})$ $\rightarrow Ar + Ar^+ + e$	$5 \times 10^{-10} T_n^{0.5}$	[30]d,e
$Ar^+ + Ar \rightarrow Ar + Ar^+$	$5.66 \times 10^{-10} T_n^{0.5}$	[24]
$Ar^+ + Ar + Ar \rightarrow Ar + Ar_2^+$	$1.41 \times 10^{-31} T_n^{-0.5} \, cm^6 \, s^{-1}$	[30]
$(Ar^*, Ar^{**}, Ar^{***}) + Ar + Ar \rightarrow Ar + Ar_2^*$	$1.14 \times 10^{-32} \, cm^6 \, s^{-1}$	[30]d,e
N_2 Reactions		
$e + N_2 \rightarrow N_2 + e$	b	[31]
$e + N_2 \leftrightarrow N_2^* + e$	b,c	[31]
$e + N_2 \leftrightarrow N_2^{**} + e$	b,c	[31]
$e + N_2 \leftrightarrow N_2^{***} + e$	b,c	[31]
$e + N_2^* \leftrightarrow N_2^{**} + e$	b,c	[31]
$e + N_2^* \leftrightarrow N_2^{***} + e$	b,c	[31]
$e + N_2^{**} \leftrightarrow N_2^{***} + e$	b,c	[31]
$e + N_2 \rightarrow N_2^+ + e + e$	b	[31]
$e + N_2^* \rightarrow N_2^+ + e + e$	b	[31]
$e + N_2^{**} \rightarrow N_2^+ + e + e$	b	[31]
$e + N_2^{***} \rightarrow N_2^+ + e + e$	b	[31]
$e + N_2 \rightarrow N + N + e$	b	[32]
$e + N_2 \leftrightarrow N_2(v) + e$	b,c	[31]f
$e + N_2(v) \rightarrow N_2(v) + e$	b	[31]f

$e + N_2(v) \leftrightarrow N_2^* + e$	b,c	[31]f
$e + N_2(v) \to N_2^+ + e + e$	b	[31]f
$e + N \to N + e$	b	[33]
$e + N \leftrightarrow N^* + e$	b,c	[34]
$e + N \to N^+ + e + e$	b	[35]
$e + N^* \to N^+ + e + e$	b	[34]
$e + N_2^+ \to N^* + N$	$2 \times 10^{-7} T_e^{-0.5}$	[36]
$e + N_4^+ \to N_2 + N_2$	$2 \times 10^{-7} T_e^{-0.5}$	[36]d
$N^* + N_2 \to N + N_2$	2.4×10^{-14}	[37]
$N_2^* + N_2 \to N_2 + N_2$	1×10^{-11}	[38]
$N_2^{**} + N_2 \to N_2 + N_2$	1×10^{-11}	[38]d
$N_2^{**} + N_2 \to N_2 + N_2$	1×10^{-11}	[38]d
$N_2^{***} + N_2 \to N_2^* + N_2$	1×10^{-11}	[38]d
$N_2^* + N_2^* \to N_2 + N_2^{**}$	1×10^{-10}	[39]
$N_2(v) + N_2 \to N_2 + N_2$	1×10^{-11}	[38]d,f
$N_2(v) + N \to N_2 + N$	1×10^{-11}	[38]d,f
$N_2^{***} + N_2^* \to N_4^+ + e$	5×10^{-11}	[40]
$N_2^{***} + N_2^{**} \to N_4^+ + e$	5×10^{-11}	[40]d
$N_2^{***} + N_2^{***} \to N_4^+ + e$	2×10^{-10}	[40]
$N^+ + N \to N + N^+$	5×10^{-12}	[41]d
$N_2^+ + N \to N_2 + N^+$	5×10^{-12}	[41]
$N_2^+ + N^* \to N_2 + N^+$	1×10^{-10}	[41]
$N_2^+ + N_2 + N_2 \to N_2 + N_4^+$	$6.8 \times 10^{-29} T_n^{-1.64} \, \mathrm{cm^6 \, s^{-1}}$	[41]
$N_4^+ + N_2 \to N_2 + N_2 + N_2^+$	$9.35 \times 10^{-13} T_n^{1.5}$	[41]
H₂O, OH, H Reactions		
$e + H_2O \to H_2O + e$	b	[42]
$e + H_2O \to H_2O(v1, 2; v3, 4) + e$	b	[42]g
$e + H_2O \to H_2O^+ + e + e$	b	[42]
$e + H_2O \to O^- + H_2$	b	[42]
$e + H_2O \to OH^- + H$	b	[42]
$e + H_2O \to OH + H + e$	b	[42]
$e + H_2O \to OH + H^* + e$	b	[42]
$e + H_2O \to OH + H^{**} + e$	b	[42]
$e + H_2O \to OH + H^{***} + e$	b	[42]
$e + H_2O \to OH^* + H + e$	b	[42]
$e + H_2O^+ \to OH + H$	$5.1 \times 10^{-8} T_e^{-0.5}$	[43]
$e + H \to H + e$	b	[44]
$e + H \leftrightarrow H^* + e$	b,c	[45]
$e + H \leftrightarrow H^{**} + e$	b,c	[45]
$e + H \leftrightarrow H^{***} + e$	b,c	[45]
$e + H^* \leftrightarrow H^{**} + e$	b,c	[45]
$e + H^* \leftrightarrow H^{***} + e$	b,c	[45]
$e + H^{**} \leftrightarrow H^{***} + e$	b,c	[45]
$e + OH \to OH^* + e$	$2.7 \times 10^{-10} T_e^{0.5}$	[46]
$e + OH^* \to O + H + e$	$1.5 \times 10^{-7} T_e^{-0.75} \exp(-3.9/T_e)$	[47]
$H_2O^+ + H_2O \to H_2O + H_2O^+$	5.1×10^{-11}	[41]d
$(H^*, H^{**}, H^{***}) + H_2O \to H + H_2O$	9.1×10^{-9}	[48]d,e
$(H^{**}, H^{***}) + H_2O \to H^* + H_2O$	9.1×10^{-9}	[48]d,e
$H^{***} + H_2O \to H^{**} + H_2O$	9.1×10^{-9}	[48]d
$OH^* + H_2O \to OH + H_2O$	9.1×10^{-9}	[48]d
$OH^- + H \to H_2O + e$	1.8×10^{-9}	[49]d
$(OH, OH^*) + H \to H_2O$	$6.87 \times 10^{-31} T_n^{-2}$	[50]d,e
$(OH, OH^*) + (OH, OH^*) + M \to H_2O_2 + M$	$6.9 \times 10^{-31} T_n^{-0.8} \, \mathrm{cm^6 \, s^{-1}}$	[50]e,j
$H_2 + HO_2 \to H_2O_2 + H$	$5 \times 10^{-11} \exp(-T_g/11310)$	[50]
$HO_2 + HO_2 \to H_2O_2 + O_2$	$8.05 \times 10^{-11} T_n^{-1}$	[50]
$HO_2 + HO_2 + M \to H_2O_2 + O_2 + M$	$1.9 \times 10^{-33} \exp(980/T_g) \, \mathrm{cm^6 \, s^{-1}}$	[50]d,j
$HO_2 + H_2O \to H_2O_2 + OH$	$4.65 \times 10^{-11} \exp(-11647/T_g)$	[50]
$H + H_2O_2 \to HO_2 + H_2$	$8 \times 10^{-11} \exp(-4000/T_g)$	[50]
$H + H_2O_2 \to OH + H_2O$	$4 \times 10^{-11} \exp(-2000/T_g)$	[50]
$O_2 + H_2O_2 \to HO_2 + HO_2$	$9 \times 10^{-11} \exp(-19965/T_g)$	[50]
$O + H_2O_2 \to HO_2 + OH$	$1.4 \times 10^{-12} \exp(-2000/T_g)$	[50]
$O^* + H_2O_2 \to O_2 + H_2O$	5.2×10^{-10}	[50]
$OH + H_2O_2 \to HO_2 + H_2O$	$2.9 \times 10^{-12} \exp(-160/T_g)$	[50]
$H_2O_2 \to OH + OH$	$1.96 \times 10^{-09} T_n^{-4.86} \exp(-26800/T_g) \, \mathrm{s^{-1}}$	[50]
$(H, H^*, H^{**}, H^{***}) + H_2O_2 \to OH + H_2O$	$4 \times 10^{-11} \exp(-2000/T_g)$	[51]d,e
$OH^- + OH^+ + M \to H_2O_2 + M$	$2 \times 10^{-25} T_n^{-2.5} \, \mathrm{cm^6 \, s^{-1}}$	h,j

(Continued).

Reaction	Rate Coefficient[a]	Ref.
$OH^- + H^+ + M \to H_2O + M$	$2 \times 10^{-25} T_n^{-2.5} \, cm^6 \, s^{-1}$	h,j
$OH^- + H_2O^+ + M \to OH + H_2O + M$	$2 \times 10^{-25} T_n^{-2.5} \, cm^6 \, s^{-1}$	h,j
$O^- + OH^+ + M \to HO_2 + M$	$2 \times 10^{-25} T_n^{-2.5} \, cm^6 \, s^{-1}$	h,j
$O^- + H^+ + M \to OH + M$	$2 \times 10^{-25} T_n^{-2.5} \, cm^6 \, s^{-1}$	h,j
$O^- + H_2O^+ + M \to O + H_2O + M$	$2 \times 10^{-25} T_n^{-2.5} \, cm^6 \, s^{-1}$	h,j
$O^- + O \to O_2 + e$	5×10^{-10}	[40]
Excitation and charge transfer		
$He^+ + H_2O \to He + H_2O^+$	6.05×10^{-11}	[52]
$He^+ + H_2O \to He + H + OH^+$	2.86×10^{-10}	[52]
$He_2^+ + H_2O \to He + He + H_2O^+$	6.05×10^{-11}	[52]d
$He_2^+ + H_2O \to He + He + H + OH^+$	2.86×10^{-10}	[52]d
$(He^*, He^{**}, He^{***}) + H_2O \to He + H_2O^+ + e$	6.6×10^{-10}	[52]d,e
$(He^*, He^{**}, He^{***}) + H_2O \to He + OH + H^+ + e$	2.6×10^{-11}	[52]d,e
$(He^*, He^{**}, He^{***}) + H_2O \to He + OH^* + H^+ + e$	2.6×10^{-11}	[52]d,e
$(He^*, He^{**}, He^{***}) + H_2O \to He + H + OH^+ + e$	1.5×10^{-10}	[52]d,e
$(He^*, He^{**}, He^{***}) + H_2O \to He + OH + H$	1.5×10^{-10}	[53]d,e
$(He^*, He^{**}, He^{***}) + H_2O \to He + OH^* + H$	1.5×10^{-10}	[53]d,e
$(He^*, He^{**}, He^{***}) + H_2O \to He + OH + H^*$	1.5×10^{-10}	[53]d,e
$(He^*, He^{**}, He^{***}) + H_2O \to He + OH + H^{**}$	1.5×10^{-10}	[53]d.e
$(He^*, He^{**}, He^{***}) + H_2O \to He + OH + H^{***}$	1.5×10^{-10}	[53]d,e
$He_2^* + H_2O \to He + He + H_2O^+ + e$	6.6×10^{-10}	[52]
$He_2^* + H_2O \to He + He + (OH, OH^*) + H^+ + e$	2.6×10^{-11}	[52]d,e
$He_2^* + H_2O \to He + He + H + OH^+ + e$	1.5×10^{-10}	[52]
$He_2^* + H_2O \to He + He + H_2O^+ + e$	6.6×10^{-10}	[53]
$He_2^* + H_2O \to He + He + OH + (H, H^*, H^{**}, H^{***})$	1.5×10^{-10}	[53]d,e
$He_2^* + H_2O \to He + He + OH^* + H$	1.5×10^{-10}	[53]d
$He^+ + O^- + M \to He + O + M$	$2 \times 10^{-25} T_n^{-2.5} \, cm^6 \, s^{-1}$	h,j
$He_2^+ + O^- + M \to He + He + O + M$	$2 \times 10^{-25} T_n^{-2.5} \, cm^6 \, s^{-1}$	h,j
$He^+ + OH^- + M \to He + OH + M$	$2 \times 10^{-25} T_n^{-2.5} \, cm^6 \, s^{-1}$	h,j
$He_2^+ + OH^- + M \to He + He + OH + M$	$2 \times 10^{-25} T_n^{-2.5} \, cm^6 \, s^{-1}$	h,j
$Ar^+ + H_2O \to Ar + H_2O^+$	1.5×10^{-10}	[41]
$Ar_2^+ + H_2O \to Ar + Ar + H_2O^+$	1.5×10^{-10}	[41]d
$(Ar^*, Ar^{**}, Ar^{***}) + H_2O \to Ar + OH + H$	4.8×10^{-10}	[54]d,e
$(Ar^*, Ar^{**}, Ar^{***}) + H_2O \to Ar + OH^* + H$	4.8×10^{-10}	[54]d,e
$Ar_2^* + H_2O \to Ar + Ar + (OH, OH^*) + H$	4.8×10^{-10}	[54]d,e
$Ar^+ + O^- + (M) \to Ar + (M) + O$	$2 \times 10^{-25} T_n^{-2.5} \, cm^6 \, s^{-1}$	h,j
$Ar_2^+ + O^- + (M) \to Ar + Ar + (M) + O$	$2 \times 10^{-25} T_n^{-2.5} \, cm^6 \, s^{-1}$	h,j
$Ar^+ + OH^- + (M) \to Ar + (M) + OH$	$2 \times 10^{-25} T_n^{-2.5} \, cm^6 \, s^{-1}$	h,j
$Ar_2^+ + OH^- + (M) \to Ar + Ar + (M) + OH$	$2 \times 10^{-25} T_n^{-2.5} \, cm^6 \, s^{-1}$	h,j
$N_2^+ + H_2O \to N_2 + H_2O^+$	2.4×10^{-9}	[41]
$N^+ + H_2O \to N + H_2O^+$	2.4×10^{-9}	[41]d
$N_4^+ + H_2O \to N_2 + N_2 + H_2O^+$	2×10^{-10}	[41]
$N_2^+ + O^- + M \to N_2 + O + M$	$2 \times 10^{-25} T_n^{-2.5} \, cm^6 \, s^{-1}$	h,j
$N_4^+ + O^- + M \to N_2 + N_2 + O + M$	$2 \times 10^{-25} T_n^{-2.5} \, cm^6 \, s^{-1}$	h,j
$N_2^+ + OH^- + M \to N_2 + OH + M$	$2 \times 10^{-25} T_n^{-2.5} \, cm^6 \, s^{-1}$	h,j
$N_4^+ + OH^- + M \to N_2 + N_2 + OH + M$	$2 \times 10^{-25} T_n^{-2.5} \, cm^6 \, s^{-1}$	h,j
$(N_2^{**}, N_2^{***}) + H_2O \to N_2 + OH + H$	4.5×10^{-10}	[55]d,e
$N_2^* + H_2O \to N_2 + OH^* + H$	4.5×10^{-10}	[55]d
Radiative Transitions		
$He^{**} \to He$	$5.7 \times 10^4 \, s^{-1}$	[50]i
$He^{***} \to He^*$	$9.5 \times 10^6 \, s^{-1}$	[50]
$He^{**} \to He^*$	$1.0 \times 10^7 \, s^{-1}$	[50]
$He_2^* \to He + He$	$1 \times 10^7 \, s^{-1}$	[56]
$Ar^{***} \to Ar^*$	$3.3 \times 10^7 \, s^{-1}$	[50]
$Ar^{***} \to Ar$	$3.1 \times 10^5 \, s^{-1}$	[50]i
$Ar^{**} \to Ar$	$5.3 \times 10^5 \, s^{-1}$	[50]i
$Ar_2^* \to Ar + Ar$	$6 \times 10^7 \, s^{-1}$	[30]
$N_2^{***} \to N_2$	$2 \times 10^5 \, s^{-1}$	[50]i
$N_2^{**} \to N_2^*$	$3 \times 10^7 \, s^{-1}$	[41]d
$N_2^{***} \to N_2^*$	$2 \times 10^6 \, s^{-1}$	[50]d
$N^* \to N$	$6 \times 10^7 \, s^{-1}$	[50]
$H^* \to H$	$4.7 \times 10^8 \, s^{-1}$	[50]
$H^{**} \to H$	$5.6 \times 10^7 \, s^{-1}$	[50]
$H^{**} \to H^*$	$4.4 \times 10^7 \, s^{-1}$	[50]

H*** → H*	$8.4 \times 10^6 \text{ s}^{-1}$	[50]
OH* → OH	$1.3 \times 10^6 \text{ s}^{-1}$	[57]
Photoionization		
$hv + H_2O \rightarrow H_2O^+ + e$	$1 \times 10^{-17} \text{ cm}^2$	[14]d

[a] Rate coefficients have unit of $cm^3 \text{ s}^{-1}$ unless noted otherwise. Electron temperature T_e is in eV. Gas temperature T_g is in K. T_n is the normalized gas temperature, $(T_g/300)$.
[b] Rate coefficient was obtained by solving Boltzmann's equation for the electron energy distribution. Cross sections for the process are from the indicated reference.
[c] Cross section and rate coefficient obtained by detailed balance.
[d] Approximated by analogy.
[e] Reactants and products in parenthesis denote the same rate coefficient was used for all species.
[f] Electron impact excitation into vibrational states 1–8 was lumped into a single vibrational state $N_2(v)$.
[g] Electron energy loss in exciting H_2O to vibrational states was included in calculation of the electron energy distribution, however $H_2O(v)$ was not explicitly followed as an excited state in the model.
[h] Charge neutralization reactions estimated independent of 3rd body.
[i] The radiation trapping factor is estimated to be 10^3–10^4 for UV and VUV emission.
[j] $M = $ He, Ar, N_2, H_2O.

are nominally H($n = 2$), H($n = 3$), H($n = 4$) and OH(A), respectively.

At atmospheric pressure, the collision frequency is sufficiently high that excitation transfer from excited states of He, Ar and N_2 to H_2O can be an important (and perhaps a dominant) method to produce excited states of H and OH. The experiments [11] measured total optical emission and selectively, using filters, optical emission from the OH($A–X$) transition at 306 nm and the H(n=3–2) transition, H_α, at 656 nm. Electron impact dissociative excitation of H_2O producing of OH(A) requires at least 9.0 eV. The dissociative excitation of H_2O producing H($n = 2$), H($n = 3$), H($n = 4$) requires 15.4 eV, 18.5 eV and 19.3 eV, respectively. Given the lower threshold for producing OH(A), excitation transfer to H_2O from any excited state of He and Ar can produce OH(A). The rate coefficients for these excitation transfer reactions are nearly gas kinetic. Excitation transfer from excited states of N_2 occurs only for $N_2(C)$ and higher states, which are likely not to be heavily populated. Excitation transfer to H_2O resulting in H_α radiation requires as a product H($n = 3$), or 18.5 eV of energy. Only He excited states have sufficient energy to do so by collisional transfer, and so H_α radiation observed from bubbles in Ar and N_2 must proceed through electron impact dissociative excitation of H_2O or direct electron impact excitation of H atoms.

We assumed that all ions neutralize on solid surfaces and return to the gas phase as their neutral counterparts, and that excited species return as their ground states. As a result, charges accumulate on non-conducting surfaces. At water surfaces, ions and neutral radicals naturally solvate with some probability and remain in the water. As an extreme case, we assumed that the water surface is absorbing for neutral radicals and ions with charge accumulating at the surface.

Tachibana [11] reported on spatially dependent total optical emission and H_α emission at 656.3 nm. The former was obtained with a digital camera without a filter with exposure over the entire discharge period. For the latter, emission was observed through a band-pass filter centred at 658 nm with a 10 nm bandwidth. Time and spatially integrated emission was also reported for H_α and OH($A–X$). In our model, the total
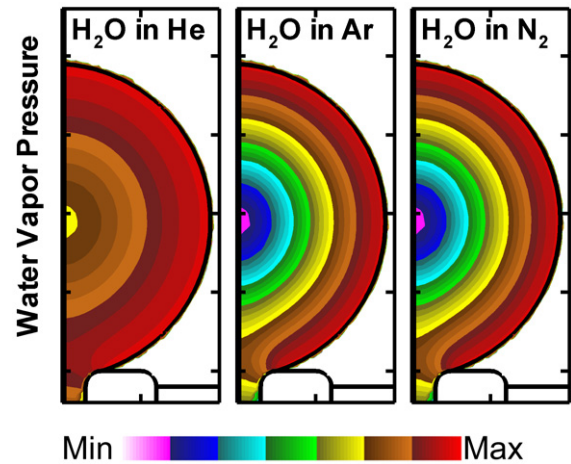

Figure 2. The density of water vapour inside the bubble after 1 ms. The density of the saturated water vapour at the water boundary is 3% of the injected gases at 300 K. The contours are plotted on a log scale over three decades.

emission for each gas mixture was synthesized by integrating over time the density of excited species emitting in the visible weighted by their corresponding Einstein A coefficients. For H_α emission, we computed the intensity by integrating over time the density of H($n = 3$) weighted by its corresponding Einstein A coefficient. The images taken in the experiment were the projection of the emission from the spherical bubble, which included contributions from individual streamers at different azimuthal locations. Our simulation is cylindrically symmetric and so a 1-to-1 correspondence with experimental images is not directly possible. However, the comparison of computed trends with experiment provides insights to the location of formation of excited states.

3. Plasmas in He, Ar and N_2 in bubbles in water

Water vapour densities in the He, Ar and N_2 bubbles at the time the voltage is applied, approximately 1 ms after bubble formation, are shown in figure 2. [H_2O] is $5.8 \times 10^{17} \text{ cm}^{-3}$ at the boundary of the bubble in each case, given by the room

temperature vapour pressure of water, 27 Torr. With the larger diffusion coefficient of H_2O in He, $[H_2O]$ is 4×10^{15} cm^{-3} in the centre of the bubble, about a factor of two larger than the density of H_2O in the centre of the Ar and N_2 bubbles. These differences in the distribution of water vapour impact the production of H and OH.

The time evolutions of electron density, n_e, electron temperature, T_e, and E/N (electric field/gas number density) during the discharge are shown in figure 3 for PBW in He, Ar and N_2 for a step function in voltage to positive 15 kV. The discharge forms and propagates in the bubble within 10 ns. The discharge starts at the tip of the powered electrode where the initial electrons are seeded, likely by emission from either the electrode or the water. The electric field is refracted towards the gas–water interface due to the curvature of bubble boundary and different dielectric constants between the gas and water, which also produces electric field enhancement [10]. Therefore, once the discharge begins, it is directed along the interface of the gas and water, as observed in the experiments of Tachibana [11] and others [8]. Charge accumulating on the surface of the interface then provides the functionality of a dielectric barrier discharge. The propagation of the surface streamer is sustained by electric field enhancement at the head of the streamer, producing maximum E/N of 4000–7000 Td (1 Td $= 10^{-17}$ V cm^2). This space charge produced electric field enhancement is in addition to the natural enhancement due to the curvature and gradient in dielectric constant, and produces T_e of 8–10 eV in Ar and N_2, and up to 35 eV in He at the leading edge of the surface hugging ionization wave. He has the largest threshold energies for electron impact excitation and ionization but with smaller cross sections, so electrons can maintain a large T_e in these large E/N. Once the discharge propagates across the inner surface of the bubble, the deposited surface charge screens out the electric field into the water at which time the T_e and ionization rates decrease. Surface hugging discharges also occur in pure, dry gases and are not necessarily correlated to the higher H_2O vapour density near the interface.

The peak electron density occurs in the vicinity of the electrode where electric field enhancement is the largest. The maximum electron densities in He and Ar are comparable, $(1–2) \times 10^{16}$ cm^{-3}, due in large part to step-wise ionization, though this is a less important factor in He since the excitation threshold is fractionally closer to the ionization threshold in He. The electron density in the N_2 bubble is about an order of magnitude smaller, a consequence of the shorter energy relaxation distance which deposits proportionately more power in non-ionizing modes (i.e. vibrational excitation). Note that the surface discharge circumnavigates the inner surface of the bubble in He and Ar within 1 ns, more quickly in He. The surface hugging ionization wave stalls before reaching the opposite pole in N_2.

The synthesized, time integrated total optical emission and H_α (656.3 nm) emission from the He, Ar and N_2 bubbles are compared to experiments [11] in figure 4. The total intensity is dominated by emission from excited states of the injected gases rather than emission from the water vapour. In the experiments, the He discharge appears to have stronger emission at the
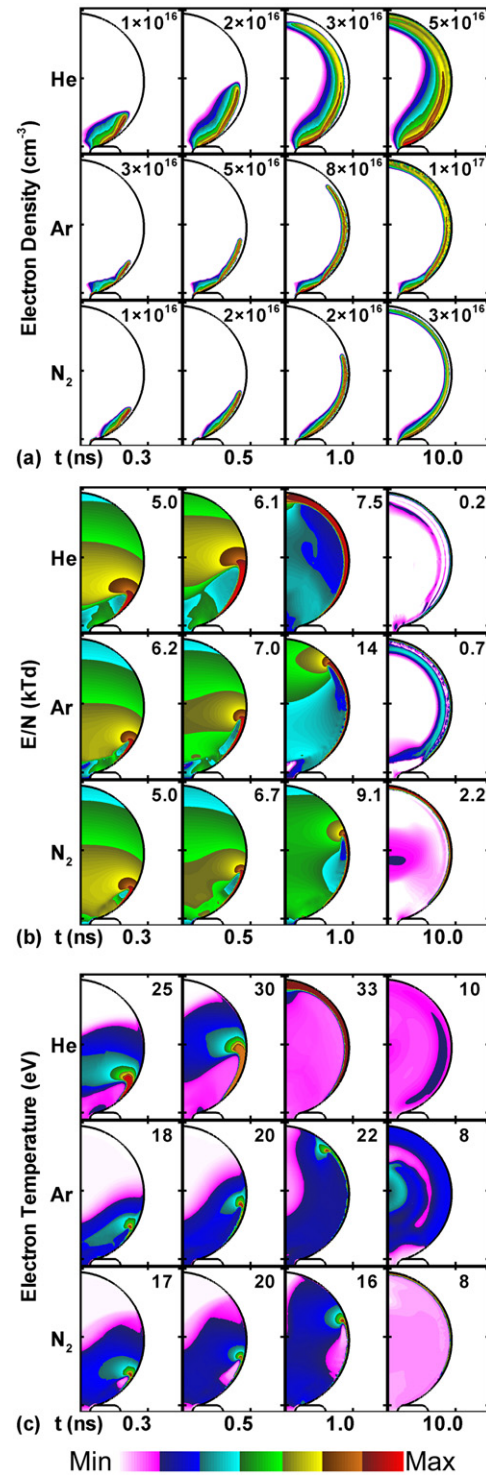

Figure 3. Time evolution of plasma properties for discharges in He, Ar and N_2 bubbles. (*a*) Electron density, (*b*) E/N and (*c*) electron temperature. The discharges are surface hugging where the electric field enhancement is the largest. The contours are plotted on a log scale over three decades with maximum values for n_e shown in each frame.

interface and to be weaker at the centre of the bubble. (Recall that the experiments are plane views of emission through the bubble and so the emission from the centre of the bubble actually contains contributions from the surface facing the observer.) The total emission in the Ar discharge appears
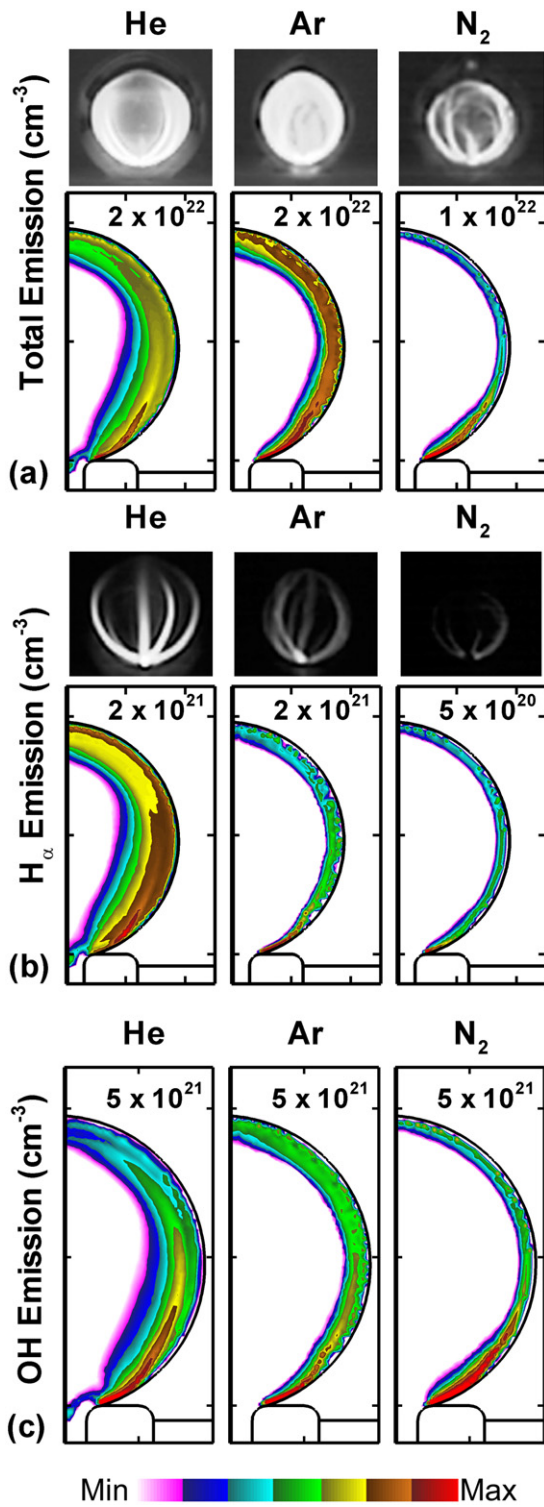
Figure 4. Time integrated emission intensity from discharges sustained in He, Ar and N$_2$ bubbles: (*a*) total visible emission, (*b*) H$_\alpha$ (656.3 nm) and (*c*) OH(*A–X*) (306.4 nm) The top row for total and H$_\alpha$ emission are images from the experiments [11]. The contours are plotted on a 3-decade log scale with the maximum values noted in each frame.

more uniform than from He but closer analysis suggests that the emission results from the contributions of many surface filaments, and not necessarily from the volume. Very clear filamentary discharge structures are observed at the surface

in the N$_2$ bubble with little optical emission from the centre of the bubble. It appears that most of the surface discharges in the N$_2$ bubble do not circumnavigate the bubble whereas the surface discharges do circumnavigate the bubbles in He and Ar.

These experimental trends for total emission are captured by the synthesized emission from the model. The predicted total emission is most uniform in the He bubble and most filamentary in the N$_2$ bubble. The emission along the surface of the gas–water interface is significantly more intense in the Ar bubble whereas the emission is weaker but deeper into the bubble for the He discharge, observations which correlate with the experiments. The total emission clearly circumnavigates the bubbles in He and Ar, and does not circumnavigate the bubble in N$_2$. The total optical emission weakly correlates with the distribution of H$_2$O vapour.

The experimental H$_\alpha$ emission intensities are significantly more confined to the surface of the bubble with contributions from individual surface streamers clearly seen in figure 4(*b*). The emission intensities are strongest from the PBW in He, weaker for Ar, and near the detection limit in the N$_2$ bubble. These trends are well reproduced by the synthesized H$_\alpha$ emission predicted by the model. In the computed results, the H$_\alpha$ emission is more volumetric from the He bubble, while the emission is confined along the interface for the Ar or N$_2$ bubbles. Since H$_\alpha$ emission comes from dissociative excitation of water vapour and excitation of its dissociation fragments, the distribution of water vapour directly contributes to the spatial distribution of the H$_\alpha$ emission. The more intense emission and somewhat more uniform emission from the He bubble has at least two sources—the H$_2$O vapour has diffused deeper into the bubble and T_e is larger, which more efficiently produces dissociative excitation of the H$_2$O. The more confined and weaker emission from PBW in N$_2$ results from the more concentrated water vapour near the boundary and the lower T_e.

The synthesized OH(*A–X*) emission is also shown in figure 4(*c*). The OH(*A–X*) emission follows the same trends as H$_\alpha$ emission—deeper into the bubble in the case of He and more confined along the interface for Ar and N$_2$. This is an expected result as the OH(*A–X*) emission similar to the H$_\alpha$ emission, ultimately originates from dissociative excitation of water vapour. However the OH(*A–X*) emission in Ar and N$_2$ bubble are stronger than H$_\alpha$. The reason will be discussed below.

The distribution of plasma and optical emission are in part explained by the electron energy relaxation lengths, λ_e, shown in figure 5 for 1 atm. These values were computed from stationary solutions of Boltzmann's equation using a 2-term spherical harmonic expansion for gases with different concentrations of water vapour [17]. The λ_e for pure water vapour is shown in each plot as a reference. The λ_e for pure gases decreases with increasing electron energy as inelastic collisions begin to dominate. λ_e for He is about 2 mm below 5–6 eV and decreases to 0.1 mm as the electron energy increases to 10 eV. The bubble is 2 mm in diameter. In Ar, λ_e is larger than 10 mm below 4 eV and quickly decreases to 0.01 mm at 8 eV. N$_2$ and H$_2$O have small λ_e, about 0.01 mm, except in the purely elastic regime at $T_e < 0.1$ eV.
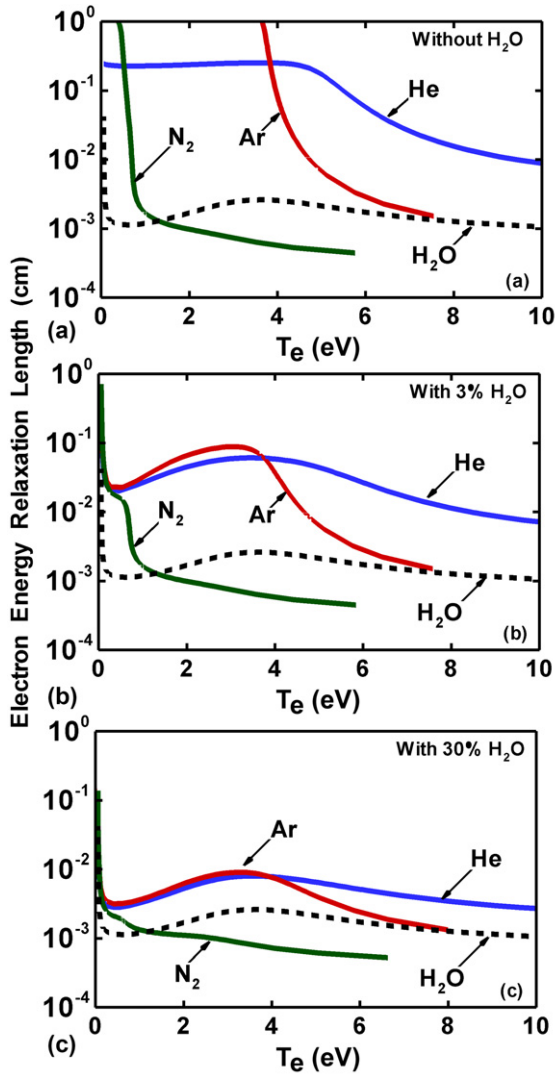
Figure 5. Electron energy relaxation length, λ_e, in He, Ar and N$_2$ at 1 atm with different water vapour concentrations. (*a*) 0%, (*b*) 3%, (*c*) 30%. Small amounts of water vapour significantly lower λ_e in He and Ar. The dotted line shows λ_e in pure water for reference.

Figure 6. Optical emission properties from discharges in bubbles. (*a*) Relative intensities of H$_\alpha$ (656.3 nm) and OH(A–X) (306.4 nm) emission from discharges sustained in bubbles of He, Ar and N$_2$ in water. Predictions from the model (solid) are compared to experiments (hashed). The intensities are normalized to the H$_\alpha$ emission intensity in He. (*b*) Fractional contributions of direct electron impact, dissociative electron impact and excitation transfer to formation of emitting states.

λ_e for gases with 3% water vapour, as shown in figure 5(*b*), represents the conditions for our PBW discharges near the water surface. λ_e in He and Ar has a significant drop at $T_e < 4$–5 eV whereas λ_e is not significantly affected in N$_2$ above 0.5 eV. For the computed range of T_e, λ_e for N$_2$ is always much smaller than the size of the bubble, so that energetic electrons are confined to the boundary of the bubble where they are accelerated by the large E/N near the interface. In Ar, λ_e drops to the thickness of the water layer as T_e increases above 4 eV. However electrons which scatter out of the dense water layer will have proportionally longer λ_e in the portion of the bubble that has less water vapour. This length approaches the size of the bubble in the purer gas. A similar trend occurs in He though λ_e is longer at higher T_e than in Ar, thereby enabling somewhat more uniform rates of excitation, as observed in the plasma density and optical emission. The differences in λ_e diminish for gas mixtures with higher fractions of H$_2$O as electron energy losses are dominated by the water, as shown in figure 5(*c*).
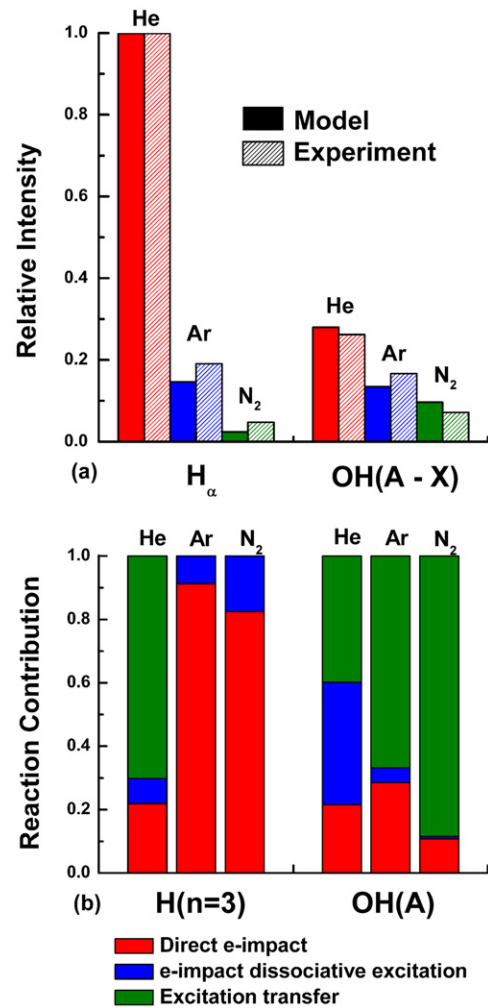
The relative volume-averaged, time integrated intensities of optical emission from excited hydrogen atoms, H$_\alpha$ (656.3 nm), and from OH(A–X) (306.4 nm) are shown in figure 6(*a*). These values were obtained from the model by performing a volume and time integral of the excited densities weighted by their spontaneous emission coefficients. The model was normalized to the experiment for H$_\alpha$ emission from the PBW in He. Both the model and the experiments show the trend that the emission from both species is most intense from PBW in He bubbles and least intense from N$_2$ bubbles. The H$_\alpha$ emission from the He bubble is significantly more intense than emission from the Ar bubble (a factor of 5), which in turn is more intense than from the N$_2$ bubble (another factor of 5). The OH(A–X) emission is overall less intense, and scales on a relative basis similarly to the H$_\alpha$ emission, with a factor of 2 decrease from He to Ar, and from Ar to N$_2$.

The production of H($n = 3$) and OH(A) comes through at least three channels—direct electron impact excitation

Table 3. Dissociative excitation reactions by electron impact and excitation transfer.

Electron impact direct excitation	
$e + H(n = 1) \rightarrow H(n = 3) + e(12.04\,eV)$	$e + OH(X) \rightarrow OH(A) + e(4.04\,eV)$
Electron impact dissociative excitation	
$e + H_2O \rightarrow H(n = 3) + OH + e(18.3\,eV)$	$e + H_2O \rightarrow H + OH(A) + e(9\,eV)$
Excitation transfer	
$He^*(19.8\,eV) + H_2O \rightarrow H(n = 3) + OH + He$	$He^*(19.8\,eV) + H_2O \rightarrow H + OH(A) + He$
	$Ar^*(11.6\,eV) + H_2O \rightarrow H + OH(A) + Ar$
	$N_2^*(11.0\,eV) + H_2O \rightarrow H + OH(A) + N_2$

Note: * The lowest excited state that is able to excitation transfer.

of ground state H($n = 1$) and OH(X), electron impact dissociative excitation of H_2O, and excitation transfer from excited electronic states of He, Ar or N_2 to H_2O. These processes are shown in table 3 with their respective threshold energies. The relative contributions of these three channels that produce H($n = 3$) and OH(A) are shown in figure 6(*b*). Excitation transfer to H_2O strongly dominates the production of OH(A) in Ar and N_2 discharges, and is nominally the highest contributor in He plasmas. The trend is nearly the reverse for excitation of H($n = 3$)—direct electron impact excitation of ground state H dominates in Ar and N_2 discharges whereas excitation transfer dominates in He discharges. The H_α line is more intense in He discharges than in Ar or N_2 discharges in part due to excitation transfer from excited states of He to H_2O, which dissociates the water and produces H($n = 3$). Excited states of Ar or N_2 are not energetic enough to produce such emission. Excited states of He, Ar and N_2 can all excitation transfer to H_2O to produce OH(A), and so the emission intensities are more nearly equal.

The average densities of the ground states H($n = 1$) and OH(X) are in the range 10^{13}–$10^{14}\,cm^{-3}$, while the peak depletion of H_2O is only about 10% near the powered electrode. This density of ground state H and OH enables significant opportunity for direct electron impact excitation. The electron impact dissociative excitation of H_2O to produce H($n = 3$) has a higher threshold energy than direct excitation of the ground state. In turn, the rate coefficient for direct excitation is larger than that for dissociative excitation of H_2O for the entire range of T_e in the plasma. As a result, the direct electron impact excitation of H($n = 1$) contributes more to the optical emission than dissociative excitation in the Ar and N_2 discharges. In He discharges, excitation transfer dominates.

The time and spatially integrated relative emission intensities for H_α and OH(A–X) as a function of applied voltage, are shown in shown in figure 7. (The discharge cannot be sustained in N_2 bubbles for voltages less than 15 kV.) The relative increase of optical emission with increasing voltage is smallest for discharges in He bubbles and greatest for discharges in N_2 bubbles. T_e increases with applied voltage in the surface hugging ionization wave but is relatively constant in the plasma column behind the ionization wave while current flows to charge the capacitance of the surface of the bubble. The increase in emission is largely due to the longer current pulse at nearly constant T_e required to charge the bubble capacitance as the voltage increases.

Production of H($n = 3$) is dominated by excitation transfer in He discharges. In Ar and N_2 discharges, production
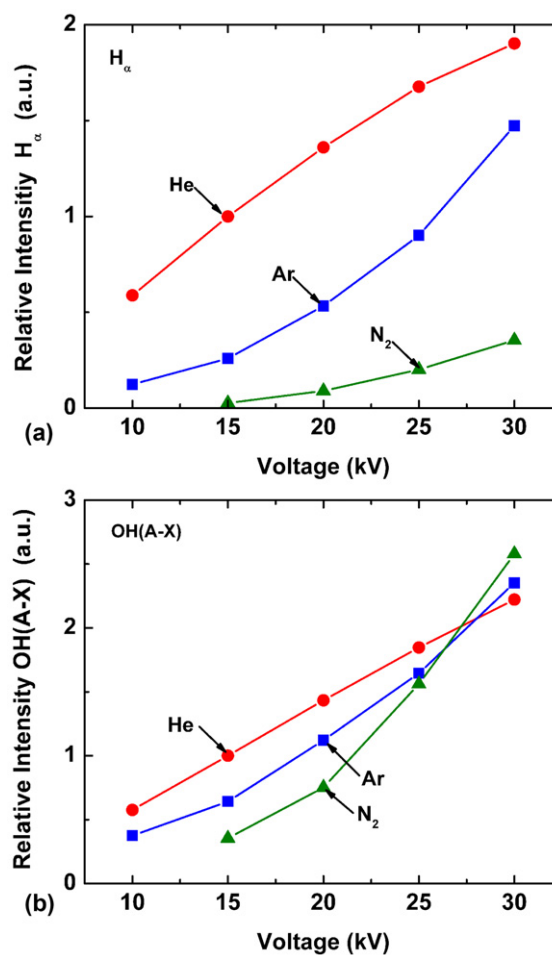

Figure 7. Time and spatially integrated intensities of (*a*) H_α (656.3 nm) and (*b*) OH(A–X) (306.4 nm) with different applied voltages. The intensities are normalized to the H_α emission intensity and OH(A–X) emission intensity in He discharge at 15 kV.

of H($n = 3$) is dominated by direct electron impact of H atoms following dissociative excitation transfer to H_2O. The accumulation of H($n = 1$) during the longer current pulse in Ar and N_2 discharges enables proportionately larger H_α emission due to the accumulation of the ground state species. Similar trends apply for OH emission where the accumulation of OH(X) enables direct electron impact excitation of OH(A). At the time of the discharge in Ar and N_2 bubbles, the water vapour is most dense near the boundary and is more confined than in the He bubbles. The discharges in Ar and N_2 bubbles also occur closer to the boundary. The disproportionate increase
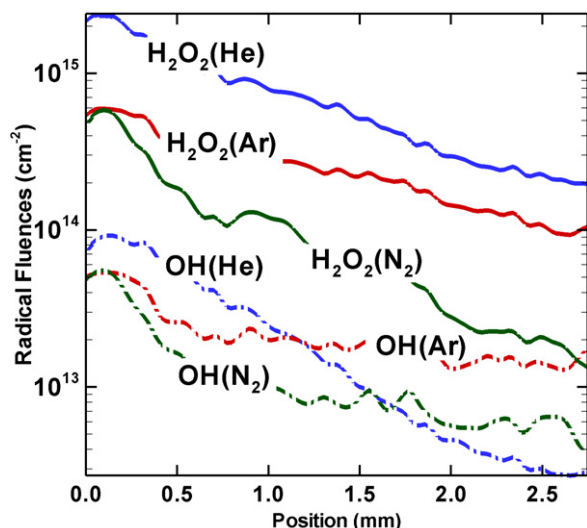
J. Phys. D: Appl. Phys. **47** (2014) 055202

Wei Tian *et al*

Figure 8. OH and H_2O_2 fluences to the bubble–water interface over a period of 1.0 s for a discharge voltage of 15 kV.

in OH($A-X$) emission that occurs in in Ar and N_2 discharges may partly result from the discharge preferentially occurring through the more dense H_2O vapour layer at the surface of the bubble.

One of the applications of plasmas in bubbles is to purify water. This purification results, in part, from the diffusion of reactive oxygen species (ROS) created in the bubble into the water. To estimate the possible effectiveness of these processes, the fluxes of OH and H_2O_2 onto the water surface were integrated as a function of time for 1 s after the discharge pulse to provide fluences (cm^{-2}). These fluences are shown in figure 8 for a discharge voltage of 15 kV as a function of position along the gas–water interface from the electrode to the top of the bubble Since energy deposition is largest near the electrode, the fluences are highest at the bottom of the bubble decreases along the surface to the top of the bubble. OH is produced by dissociation of H_2O (by electron impact or excitation transfer) and its density exceeds that of H_2O_2 during the short discharge pulse. However, after the discharge pulse, OH is consumed by its mutual reaction in the gas phase in formation of H_2O_2 resulting in the H_2O_2 fluences generally being one-order of magnitude larger than the OH fluences. The largest H_2O_2 fluences are produced by discharges He bubbles, in large part because the electron temperature is the highest which then produces the highest rates of H_2O dissociation. Discharges in N_2 bubbles generally produce the smallest fluences of H_2O_2 due to the disproportionate amount of power spent in non-dissociative modes.

Virtually all of the positive ions striking the surface of the water undergo charge exchange with liquid H_2O to produce H_2O^+ which then quickly charge exchanges to make H_3O^+ and OH. The H_3O^+ acidifies the water and the OH dominantly forms H_2O_2. Although these sources are important in many circumstances, for our conditions the fluences of charged species onto the surface of the water are lower than those for neutral species by about a factor of 10^3.

4. Concluding remarks

The properties of pulsed discharges in He, Ar and N_2 bubbles in water were computationally investigated and the results are compared to experiments [11]. The discharges typically propagate along the surface of the where the gradient in dielectric constant is largest, producing electric field enhancement. The diffusion of water vapour into the bubble requires a finite time and so the gas adjacent to the gas–water interface has a higher density of H_2O than in the interior, which is coincidentally where the discharge also propagates. The optical emission from the bubbles reflects these discharge patterns, being more uniform in the He filled bubble where electron energy relaxation lengths are longer, and more confined along the interface for N_2 bubbles where the energy relaxation length is smallest. Total optical emission is more volumetrically distributed (though heavily weighted towards the boundary), while H_α and OH($A-X$) emissions are generally confined to the surface where both the H_2O vapour density and electron temperature are largest. The formation of OH(A) is dominated by dissociative excitation transfer to H_2O from excited states of He, Ar and N_2. The formation of H($n = 3$) is dominated by electron impact excitation of ground state H in Ar an N_2 discharges, and dissociative excitation transfer to H_2O in He discharges. For otherwise the same conditions the emission of intensities and ROS fluences to the bubble–water surface are largest in He bubbles. These results suggest that some degree of optimization or customization of radical production from PBW is possible by choice of the gas forming the bubble.

Acknowledgments

References

[1] Locke B R and Shih K-Y 2011 *Plasma Sources Sci. Technol.* **20** 034006

[2] Dobrynin D, Fridman A and Starikovskiy A Y 2012 *IEEE Trans. Plasma Sci.* **40** 2163

[3] Malik M A, Ghaffar A and Malik S A 2001 *Plasma Sources Sci. Technol.* **10** 82

[4] Burlica R, Kirkpatrick M J and Locke B R 2006 *J. Electrost.* **64** 35

[5] Kong M G, Kroesen G, Morfill G, Nosenko T, Shimizu T, Dijk J V and Zimmermann J L 2009 *New J. Phys.* **11** 115012

[6] Starikovskiy A, Yang Y, Cho Y I and Fridman A 2011 *Plasma Sources Sci. Technol.* **20** 024003

[7] An W, Baumung K and Bluhm H 2007 *J. Appl. Phys.* **101** 053302

[8] Foster J, Sommers B S, Gucker S N, Blankson I M and Adamovsky G 2012 *IEEE Trans. Plasma Sci.* **40** 1311

[9] Aoki H, Kitano K and Hamaguchi S 2008 *Plasma Sources Sci. Technol.* **17** 025006

[10] Babaeva N Y and Kushner M J 2009 *J. Phys. D: Appl. Phys.* **42** 132003

[11] Tachibana K, Takekata Y, Mizumoto Y, Motomura H and Jinno M 2011 *Plasma Sources Sci. Technol.* **20** 034005

J. Phys. D: Appl. Phys. **47** (2014) 055202

Wei Tian *et al*

[12] Babaeva N Y, Ning N, Graves D B and Kushner M J 2012 *J. Phys. D: Appl. Phys.* **45** 115203

[13] Xiong Z, Robert E, Sarron V, Pouvesle J-M and Kushner M J 2012 *J. Phys. D: Appl. Phys.* **45** 275201

[14] Hudson R D 1971 *Rev. Geophys. Space Phys.* **9** 305

[15] NIST Thermophysical Properties of Fluid Systems [Online] Available: http://webbook.nist.gov/chemistry/fluid/

[16] Hirschfelder J, Curtiss C F and Bird R B 1954 *Molecular Theory of Gases and Liquids* (New York: Wiley)

[17] Morgan W L and Penetrante B M 1990 *Comput. Phys. Commun.* **58** 127

[18] Deloche R, Monchicourt P, Cheret M and Lambert F 1976 *Phys. Rev.* A **13** 1140

[19] Alves L L, Gousset G and Ferreira C M 1992 *J. Phys. D: Appl. Phys.* **25** 1713

[20] Rapp D and Englander-Golden P 1965 *J. Chem. Phys.* **43** 1464

[21] Vriens L 1964 *Phys. Lett.* **8** 260

[22] Bekefi G 1966 *Radiation Processes in Plasmas* (New York: Wiley)

[23] Emmert F, Angermann H H, Dux R and Langhoff H 1988 *J. Phys.* D **21** 667

[24] Ellis H W, Pai R Y and McDaniel E W 1976 *At. Data Nucl. Data Tables* **17** 177

[25] Wang Q, Economou D J and Donnelly V M 2006 *J. Appl. Phys.* **100** 023301

[26] Tachibana K 1986 *Phys. Rev.* A **34** 1007

[27] Zapesochyni I P and Shimon L L 1966 *Opt. Spectrosc.* **11** 155

[28] McFarland R H and Kinney J D 1965 *Phys. Rev.* **137** 1058

[29] Biondi M A 1976 *Principles of Laser Plasmas* ed G Bekefi (New York: Wiley)

[30] Kannari F, Suda A, Obara M and Fujioka T 1983 *IEEE J. Quantum Electron.* **19** 1587

[31] Itikawa Y, Hayashi M, Ichimura A, Onda K, Sakimoto K, Takayanagi K, Nakamura M, Nishimura H and Takayanagi T 1986 *J. Phys. Chem. Ref. Data* **15** 985

[32] Phelps A V and Pitchford L C 1985 *Phys. Rev.* **31** 2932

[33] Geltman S 1973 *J. Quant. Spectrosc. Radiat. Transfer* **13** 601

[34] Henry R, Burke P G and Sinfailam A-L 1969 *Phys. Rev.* **178** 218

[35] Smith A 1962 *Phys. Rev.* **127** 1647

[36] Brian J and Mitchell A 1990 *Phys. Rep.* **186** 215

[37] Person J C and Ham D O 1988 *Int. J. Radiat. Appl. Instrum.* **31** 1

[38] Piper L G 1987 *J. Chem. Phys.* **87** 1625

[39] Piper L G 1988 *J. Chem. Phys.* **88** 231

[40] Kossyi A, Kostinsky A Y, Matveyev A A and Si V P 1992 *Plasma Sources Sci. Technol.* **1** 207

[41] Ikezoe Y, Matsuoka S, Takebe M and Viggiano 1987 *Gas Phase Ion–Molecule Reaction Rate Constants Through 1986* (Tokyo: Ion Reaction Research Group of the Mass Spectroscopy Society of Japan)

[42] Itikawa Y and Mason N 2005 *J. Phys. Chem. Ref. Data* **34** 1

[43] Rowe B R, Vallee F, Queffelec J L, Gomet J C and Morlais M 1988 *J. Chem. Phys.* **88** 845

[44] Banks P 1966 *Planet. Space Sci.* **14** 1085

[45] Janev R K, Langer W D, Evans D J and Post D E 1987 *Elementary Processes in Hydrogen and Helium Containing Plasmas* (Berlin: Springer)

[46] Joshipuru K N, Vinodkumar M and Patel U M 2001 *J. Phys. B: At. Mol. Opt. Phys.* **34** 509

[47] Riahi R, Teulet P, Lakhdar Z B and Gleizes A 2006 *Eur. Phys. J.* D **40** 223

[48] Quickenden T I, Trotman S M, Irvin J A and Sangster D F 1979 *Chem. Phys.* **71** 497

[49] Madden K P and Mezyk S P 2011 *J. Phys. Chem. Ref. Data* **40** 023103

[50] 'NIST Chemical Kinetics Database.,' [Online]. Available: http://kinetics.nist.gov/kinetics/index.jsp

[51] Gordillo-Vazquez F J 2008 *J. Phys. D: Appl. Phys.* **41** 234016

[52] Miller T J, Farquhar P and Willacy K 1997 *Astron. Astrophys. Suppl. Ser.* **121** 139

[53] Sanders R A and Muschlitz E E 1977 *Int. J. Mass Spectrosc. Ion Phys.* **23** 99

[54] Jong H D 1974 *Chem. Phys. Lett.* **25** 129

[55] Pancheshnyi S V, Starikovskaia S M and Starikovskii A Y 2000 *Chem. Phys.* **262** 349

[56] Naidis G V 2011 *J. Phys. D: Appl. Phys.* **44** 215203

[57] Binns W R and Ahl J L 1978 *J. Chem. Phys.* **68** 538